Enhanced Evanescent Field via Integration of Graphene Oxide/PMMA Hybrid Film on Coreless D-shaped Fibers

BING SUN,[1, 2, 4] KAI WAN,[1] KAIMING ZHOU, [2] ZHENDONG HUANG, [3] ZUXING ZHANG[1, 5]

[1]*Advanced Photonic Technology Lab, College of Electronics and Optical Engineering & College of Flexible Electronics (Future Technology), Nanjing University of Posts and Telecommunications, Nanjing 210023, P. R. China*

[2]*Aston Institute of Photonic Technologies, Aston University, Birmingham B4 7ET, UK*

[3]*State Key Laboratory for Organic Electronics and Information Displays & Jiangsu Key Laboratory for Biosensors, Institute of Advanced Materials (IAM), Jiangsu National Synergetic Innovation Center for Advanced Materials (SICAM), Nanjing University of Posts and Telecommunications, Nanjing 210023, P. R. China*

[4]b.sun@njupt.edu.cn

[5]zxzhang@njupt.edu.cn

Received XX Month XXXX; revised XX Month, XXXX; accepted XX Month XXXX; posted XX Month XXXX (Doc. ID XXXXX); published XX Month XXXX

This study presents the implementation of an evanescent field-based sensing platform employing a hybrid film composed of graphene oxide and poly(methyl methacrylate) (PMMA), integrated onto coreless D-shaped fibers (*c*D*s*Fs). The operational framework of the hybrid film-coated *c*D*s*Fs (GoP-*c*D*s*Fs) was comprehensively elucidated through theoretical and experimental analyses. To establish a baseline for comparison, the performance of the cDsFs with the sole inclusion of the PMMA film was investigated. Our investigations underscore the substantive role of graphene oxide in augmenting the evanescent field, thereby generating a synergistic effect that contributes to the overall enhancement of the evanescent field in the device. Consequently, the fabricated GoP-*c*D*s*F sensor manifests an outstanding sensitivity of -4.936 nm/°C, rendering it particularly well-suited for applications demanding high-sensitivity temperature sensing. Moreover, the unique attributes of the GoP-*c*D*s*F position it as a promising candidate for the measurement of both magnetic and electric fields, presenting an effective strategy for multifunctional sensing applications.

Evanescent field-based sensing, in particular, plays a vital role in detecting changes in the surrounding medium by exploiting the interaction between the evanescent field and the analyte. The evanescent field (EF) extends beyond the core of the optical fiber and interacts with the surrounding medium, making it a crucial component for efficient sensing [1-3]. Undoubtedly, the utilization of micro/nano fibers is known to generate a robust evanescent field within the confined region [4-8]. An intriguing alternative approach involves the implementation of D-shaped structures with adjustable residual thickness, which holds great promise for enhancing the evanescent field and thereby showcasing its potential in sensing applications [9-10]. Notably, the presence of macro scratches on the rough polished surface has been demonstrated to achieve a Mach-Zehnder interference spectrum [11]. As an alternative, it is worth acknowledging that the D-shaped structure with coating techniques, such as the use of noble metals, dielectric layers, and nanoparticles, present opportunities for further enhancing the EF [12-18].

Optical fiber sensing technologies (OFSTs) have witnessed a remarkable transformation in the realm of nanotechnology, owing to the remarkable properties and versatile applications of two-dimensional materials, such as graphene oxide. One intriguing phenomenon associated with these materials is the unprecedented enhancement of the EF, propelling the advancement of OFSTs to new heights [15, 17-18]. The exceptional attributes of graphene oxide empower it to augment the EF within optical fibers, resulting in highly sensitive and precise sensing capabilities. Zhuo et al. [19] reported the integration of the monolayer graphene onto the side-polished optical fiber to enhance the light–graphene interaction, then improving the optical absorption of monolayer graphene to 65.53%. For instance, a high-sensitivity and fast-response fiber-optic plasmonic temperature sensor is developed by coating graphene and polydimethylsiloxane onto an optical-fiber based plasmonic interface [15]. Wu et al. demonstrate and verify the efficacy of an optical gas sensor that leverages graphene-induced enhancement of evanescent fields and an in-fiber multimode interferometer [20]. This innovative design exhibits exceptional sensitivity to the adsorption of polar gas molecules, showcasing remarkable performance.

On the other hand, the temperature sensitivity employed in the common fiber-optic sensing schemes is typically limited to a few dozens of picometers per degree Celsius (pm/°C) due to the low thermal optical coefficient of quartz material [21]. To overcome this limitation and enhance sensitivity, researchers have explored the

use of coating materials with higher thermal optical coefficients [22-24]. For instance, Wu et al. reported a fiber temperature senor by wrapping the sensitive material PDMS and realized a high sensitivity of −0.4409 nm/°C [25]. Nevertheless, considering the thermal optic coefficient (TOC) of PDMS (−4.66×10⁻⁴/°C), there is potential for even greater sensitivity.

In this Letter, we leverage a coreless D-shaped fiber (*c*D*s*F) coating with PMMA (poly(methyl methacrylate)) to amplify the evanescent field through the utilization of graphene oxide (GO). Notably, the composite material involving reduced graphene oxide and PMMA discussed in Ref. [26] culminates in the formation of a singular film. Conversely, our investigation encompasses the fabrication of two distinct films: a GO film and a PMMA film. Through theoretical calculations, we compare the field penetration into the PMMA in the presence and absence of GO, demonstrating notable enhancements. Additionally, we conduct experimental investigations, discerning distinct performance characteristics between the schemes with and without GO. We measure the temperature sensitivity of the GoP-incorporated schemes to be -4.936 nm/°C. Furthermore, this method can area-selectively deposit desired GO around cDsF, and can be realized by a simple process and setup.

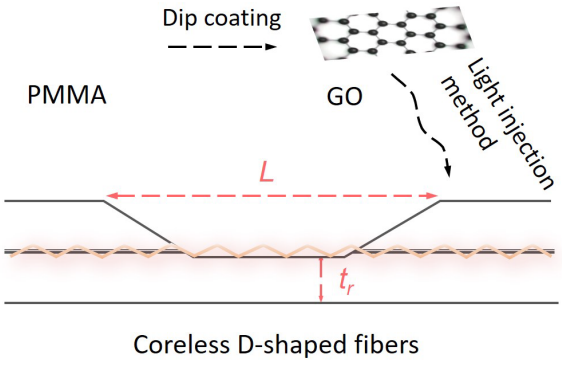

Fig. 1. Fabrication process of the as-fabricated structure.

Figure 1 indicates the three-dimensional structure of the cladding-side polished fiber-based sensor. By wheel side-polishing technique, a single-mode fiber is polished into a coreless guiding region with a D-shaped cross section by removing part of the optical fiber [25, 27]. Through a comprehensive comparative analysis, it has been ascertained that samples characterized by specific parameters, namely, t_r = 50 μm and L = 5 mm, exhibit a noteworthy suitability for subsequent experiments (refer to Fig. S1 in the supplementary material). This suitability arises from the observation that these parameters result in a reduced number of modes involved in interference phenomena, thereby yielding an exceptionally favorable transmission spectrum. The GO was then transferred to the *c*D*s*F by an optical deposition method [28-29]. As a sensitivity-enhanced coating material, the PMMA film with a refractive index of ~1.48 higher than the fiber has been further demonstrated for significantly enhancing the temperature sensitivity in case that the light enters the PMMA coating with a high TOC with the help of GO.

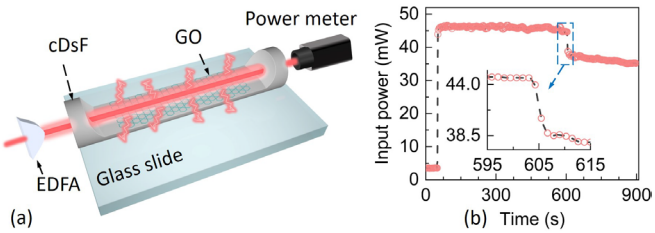

Fig. 2. (a) Experimental setup for GO deposition around the *c*D*s*F by light injection method. (b) Deposition process using ethanol as solvent.

An ultra-large GO dispersion was synthesized utilizing a modified Hummer's method [30], which involves a sequential four-step process for preparing the ultra-large GO. Firstly, the *c*D*s*F was soaked in the deposited ethanol aqueous solution of ultra-large GO. Upon injecting a continuous wave laser at 1550 nm with an average power of 1 W into the *c*D*s*F through an erbium-doped fiber amplifier (EDFA) and maintaining it for a duration of 15 minutes, the output power was continuously monitored using a power meter to facilitate the control of the GO deposition time. As depicted in Fig. 2(a), a considerable enhancement (~45 mW) in the output power was observed at the ethanol droplet. While the output power remained stable over time, a sudden decrease was observed after 10 minutes, signifying the successful deposition of GO on the *c*D*s*F's surface, as shown in Fig. 2(b). The GO coating effectively served as a cladding for the *c*D*s*F. This behavior is attributed to the strong absorption characteristics of the GO film within the wavelength band.

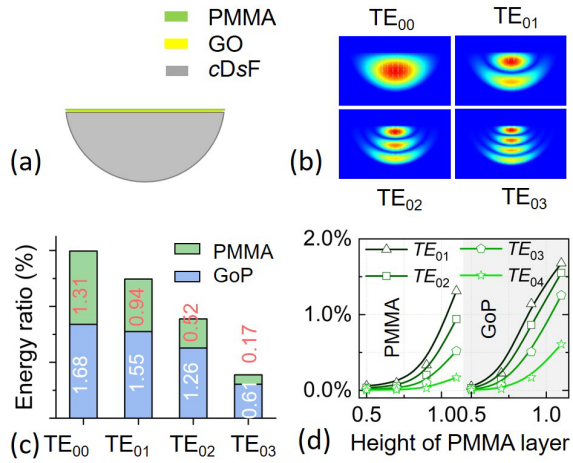

Fig. 3. (a) cross-sectional view of the as-fabricated GoP-*c*D*s*F. (b) Simulated mode distributions of the *c*D*s*F integrated with the hybrid film. (c) Comparison of energy ratios with the single PMMA and hybrid film (d) Detailed energy ratio during (c).

Considering the symmetrical attributes of the input field, denoted as $E_{in}(r,\theta)$, which originates from the fundamental mode of the lead-in single-mode fiber (SMF), the dominant excitation within the cladding-side polished fiber (see its cross-section in Fig. 3(a)) mainly comprises of $TE_{0,n}$ and $TM_{0,n}$ modes. As a result, the vectorial aspects can be reasonably neglected, permitting the representation of $TE_{0,n}$ and $TM_{0,n}$ mode fields through a scalar function, denoted as $\Psi_{0,n}(r, \theta)$. The evolution of the optical field along the planar segment

of the cladding-side polished fiber is dictated by the interference occurring among the excited higher-order modes [9]:

$$E(r,\theta,z)=\sum_{n=1}^{N} b_{0,n}\Psi_{0,n}(r,\theta)\exp(j\beta_{0,n}z). \qquad (1)$$

where $\beta_{0,n}$ is the propagation constant of $TE_{0,n}$ and $TM_{0,n}$ modes in the flat section.

The field distributions of $TE_{0,n}$ and $TM_{0,n}$ modes exhibit similarity. To simplify the analysis, we solely focus on the $TE_{0,n}$ modes while disregarding the polarization effect. In Fig. 3(b), we present the field distributions corresponding to $TE_{0,n}$ modes (n=0~3) within the flat section of the *c*DsF with t_r =52 μm. It is evident that the energy penetration into the single PMMA film depends on its height, with higher-order modes exhibiting more evanescent fields. Significantly, as depicted in Fig. 3(c), simulations have facilitated the deduction that the integration of the GO film as elucidated in reference [31], yields favorable outcomes by enhancing the penetration of the evanescent field into the PMMA film. A thorough analysis of the PMMA film height is delineated in Fig. 3(d). It is noteworthy that the SEM is employed for characterizing the thickness of the GO film transferred onto the optical fiber surface at the micron level (refer to Fig. S3 in the supplementary material). The potential disparity between the experimentally observed structure and the simulated model constitutes a subject we are poised to investigate in future research endeavors.

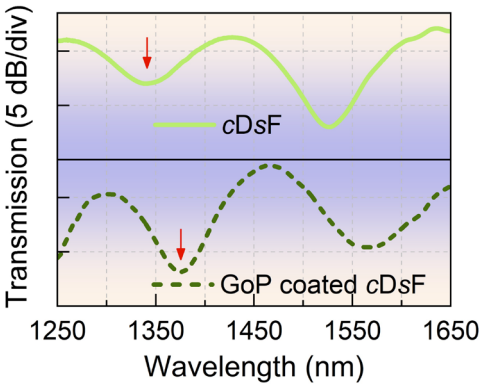

Fig. 4. Transmittance of the *c*DsF with and without the hybrid film.

Figure 4 presents a comparative analysis of the transmittance characteristics of the *c*DsF with and without the incorporation of a hybrid film. In the absence of the hybrid film, the original cDsF exhibits significant transmission interference. This high insertion loss is attributed to the modal interference caused by the absence of the fiber core, as evident from the upper part of Fig. 3. Additionally, two distinct loss dips are observed at wavelengths of 1330 nm and 1470 nm, respectively, owing to cladding modal interferences. However, upon integration of the GoP hybrid layer onto the *c*DsF, notable 'red' shifts of the loss dips are observed, measuring approximately 45 nm and 50 nm, respectively. In a qualitative assessment, the incorporation of the GoP film results in an elevation of the external refractive index of the waveguide (*c*DsF) as compared to the surrounding air, thereby inducing a discernible 'red' shift in the resonant wavelength. Concurrently, a decrease in the overall transmission loss is observed, indicative of the existence of an ancillary waveguiding mechanism, namely, the GoP hybrid film, which facilitates the propagation of light.

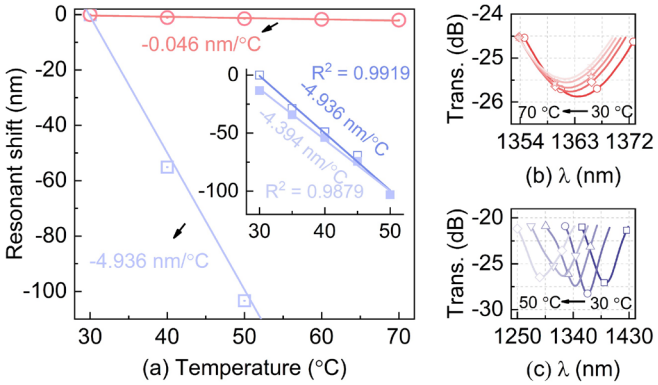

Fig. 5. (a) The dip shift as a function of the temperature. Circle-dotted line represents the temperature sensitivity of pure *c*DsF, while the Square-dotted line indicates the temperature sensitivity of the proposed sensor. (b) and (c) depict the corresponding spectra.

To investigate the evanescent field enhancement effect of the GoP-*c*DsF, we conducted a study on the modulation spectra in relation to the temperature (the interrogation system and its setup in Fig. S2 of the supplementary material). In Fig. 5, we present the thermotic spectral distributions through a specialized GoP-*c*DsF structure while systematically varying the temperature. The observed spectral shifts in the loss dip of the transmission spectra are of particular interest, as shown in Fig. 5 (b) and (c). As the temperature increased, a 'blue' shift in the loss dip was observed, demonstrating a sensitivity of -4.936 nm/ºC. Conversely, upon decreasing the temperature, a significant 'red' shift of 92.3 nm, from 1286.4 to 1378.7 nm (see the inset in Fig. 5(a)), was observed with a sensitivity of -4.394 nm/ºC in the transmitted loss dip. By comparison, the thermotic tuning of the *c*DsF (-0.046 nm/ºC) is two orders of magnitude lower than that of the proposed GoP-*c*DsF. These findings highlight the potential of the as-fabricated GoP-*c*DsF for applications where temperature-dependent modulation characteristics are crucial.

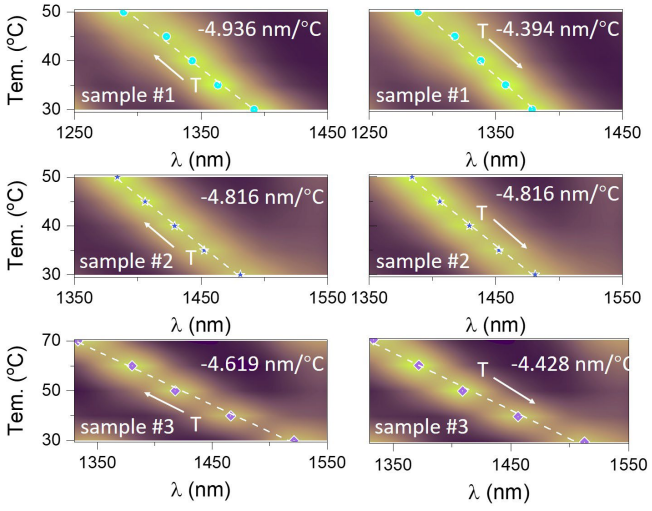

Fig. 6. Thermo-optical modulation spectral distributions of three samples.

Furthermore, we present an experimental investigation concerning the evolution of transmission spectra for three samples

using a consistent fabrication procedure. The evident similarities observed in these samples can be attributed to their identical fabrication conditions. Subsequently, we conduct a temperature test on the samples, which reveals analogous spectral trends. These measurement results can be ascribed to the variation in refractive index of the hybrid film when subjected to external temperature changes, leading to observable 'blue' shifts in the dips. The corresponding sensitivities for the samples, as depicted in Fig. 6, are found to be -4.936 nm/ºC, -4.816 nm/ºC, and -4.619 nm/ºC, respectively. The slight disparities in these sensitivities may be attributed to specific variations in the status of the hybrid film. Furthermore, a comparative analysis is conducted on the efficacy of sample #3 both pre and post a one-month duration, as delineated in Fig. S4 of the supplementary material).

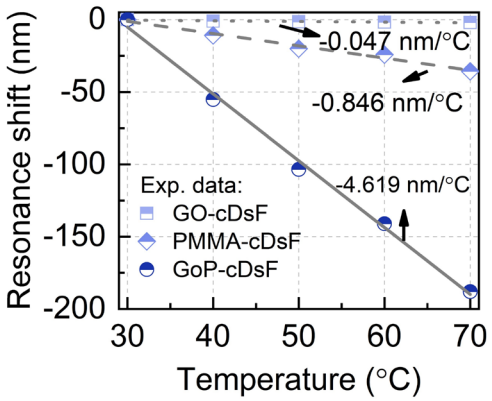

Fig. 7. The dip shifts as a function of the temperature. Circle-dotted, pentagram-dotted and square-dotted lines represents the temperature sensitivity of GoP, PMMA and GO coated cDsF, respectively.

The introduction of a GO film has been implemented to amplify the evanescent potential field situated at the surface of the *c*D*s*F, aligning seamlessly with our projected outcomes. Consequently, the incorporation of the GO film is not expected to exert a substantial influence on the enhancement of temperature sensitivities. Rather, the GO film assumes a pivotal role as an 'intermediary,' bolstering the interaction between the evanescent field and the PMMA film. As illustrated in Fig. 7, a series of experiments were conducted to investigate the interference spectra pertinent to temperature sensing within the *c*D*s*F, featuring a singular GO film coating. Notably, Fig. 3 reveals that, in the presence of the PMMA film, a fraction of the energy resides within the PMMA material, revealing a sensitivity of -0.846 nm/ºC. This contrasts with previous research involving PDMS [27], attributed to the distinct refractive indices of PDMS and the optical fiber material.

In summary, we demonstrate an evanescent field-enhancement platform with a GoP hybrid film layer integrated on the *c*D*s*F. The as-fabricated GoP-*c*D*s*F can be used as a high-sensitivity temperature sensor with sensitivities of several nanometers per degree, which is comparable to the state-of-the-art fiber-optic sensors. We believe that our work can provide a strategy for designing multifunctional devices in optical communications and sensing.

Funding. This work was supported in part by National Natural Science Foundation of China under Grants 91950105 and 62175116, in part by Outstanding Chinese and Foreign Youth Exchange Program of China Association for Science and Technology (CAST), in part by the Association Youth Science and Technology Talent Promotion (TJ219043), in part by the 1311 Talents Program of Nanjing University of Posts and Telecommunications (Dingxin), in part by the Science Foundation of Nanjing University of Posts and Telecommunications (NY222139), and in part by Marie Skłodowska-Curie Individual Fellowships in the European Union's Horizon 2020 Research and Innovation Programme under Grant 891685.

Disclosures. The authors declare no conflicts of interest.

References

1. F. Long, M. He, H.C. Shi, et al., Biosens. Bioelectron. **23**, 952-958 (2008)
2. N. Zhong, Z. Wang, M. Chen, et al., Sensor. Actuator. B Chem. **254**, 133-142 (2018).
3. Y. Song, L. Ling, P. Westerhoff, et al., Nat Commun **12**, 4101 (2021)
4. L. Zhang, J. Lou, L. Tong, Photonic Sens **1**, 31–42 (2011)
5. G. Salceda-Delgado, D. Monzon-Hernandez, A. Martinez-Rios, et al., Opt. Lett. **37**, 1974 (2012).
6. Y. Xue, Y. S. Yu, R. Yang, et al., Opt. Lett. **38**, 1209 (2013)
7. Y. Li, S. Tan, L. Yang, L. Li, et al., Adv. Fiber Mater. **4**, 226-234 (2022).
8. L. Yang, Y. Li, F. Fang, et al., Opto-Electron Adv **5**, 200076 (2022).
9. H. Dong, L. Chen, J. Zhou, et al., Opt. Express **25**, 5352-5365 (2017).
10. J. Dong, H. Huang, P. Wu, et al., Opt. Express **25**, 32504-32513 (2017).
11. J. Zhao G. Yin, C. Liao, et al., IEEE Photonics Journal 7, 1-7 (2015).
12. J. Tang, J. Zhou, J. Guan, et al., IEEE J Sel Top Quant **23**, 238-245, (2017).
13. T. Wu, Y. Shao, Y. Wang, et al., Opt. Express **25**, 20313-20322 (2017).
14. Z. Jiang, J. Dong, S. Hu, et al., Opt. Lett. **43**, 4743-4746 (2018).
15. L. Dong, X. Liu, Y. Zhang, et al., ACS Appl. Electron. Mater. **2**, 447-455 (2020).
16. C. Teng, S. Ying, R. Min, et al., Sensors **22**, 6241, (2022).
17. Q. Huang, L. Zhong, J. Dong, et al., Opt. Lett. **47**, 1478-1481 (2022).
18. Y. Wang, Y. Li, Y. Li, et al., Photon. Res. **11**, A1-A9 (2023).
19. L. Zhuo, P. Fan, S. Zhang, et al., Photon. Res. **8**, 1949-1957 (2020)
20. Y. Wu, B. C. Yao, A. Q. Zhang, et al., Opt. Lett. **39**, 6030-6033 (2014).
21. E. Li, X. Wang, and C. Zhang, Appl. Phys. Lett. **89**, 091119 (2006).
22. S. Silva, E. G. P. Pachon, M. A. R. Franco, et al., Appl. Opt. **51**, 3236–3242 (2012).
23. P. Hu, Z. Chen, M. Yang, et al., Sensors and Actuators A: Physical **223**, 114–118 (2015).
24. H. Fukano, D. Watanabe, and S. Taue, IEEE Sens. J. **16**, 8921–8927 (2016).
25. C. He, J. Fang, Y. Zhang, et al., Opt. Express **26**, 9686-9699 (2018).
26. Satyendra K. Mishra, Sandeep N. Tripathi, Veena Choudhary, et al., Sensors and Actuators B: Chemical 199, 190-200 (2014)
27. B. Sun, F. Li, K. Xu, et al., IEEE Photon. Technol. Lett. **34**, 165-168, (2022).
28. K. Kashiwagi and S. Yamashita, Opt. Express 17, 18364-18370 (2009)
29. H. Wang, B. Chen, X. Zhang, J. Wang, K. Wu and J. Chen, 2015 Opto-Electronics and Communications Conference (OECC), Shanghai, China, 2015, pp. 1-3
30. Z. Huang, H. Lu, K. Qian, et al., Nano Energy 51, 137-145 (2018).
31. S. Gan, W. Chong, C. Lai, et al., Appl. Opt. 61, 744-750 (2022)

References

1. F. Long, M. He, H.C. Shi, A.N. Zhu, “Development of evanescent wave all-fiber immunosensor for environmental water analysis,” Biosens. Bioelectron. **23**, 952-958 (2008)
2. N. Zhong, Z. Wang, M. Chen, X. Xin, R. Wu, Y. Cen, Y. Li, “Three-layer-structure polymer optical fiber with a rough inter-layer surface as a highly sensitive evanescent wave sensor,” Sensor. Actuator. B Chem. **254**, 133-142 (2018).
3. Y. Song, L. Ling, P. Westerhoff, C. Shang, “Evanescent waves modulate energy efficiency of photocatalysis within TiO_2 coated optical fibers illuminated using LEDs,” Nat Commun **12**, 4101 (2021)
4. L. Zhang, J. Lou, L. Tong, “Micro/nanofiber optical sensors,” Photonic Sens **1**, 31–42 (2011)
5. G. Salceda-Delgado, D. Monzon-Hernandez, A. Martinez-Rios, G. A. Cardenas-Sevilla, and J. Villatoro, “Optical microfiber mode interferometer for temperature-independent refractometric sensing,” Opt. Lett. 37, 1974 (2012).
6. Y. Xue, Y. S. Yu, R. Yang, C. Wang, C. Chen, J. C. Guo, X. Y. Zhang, C. C. Zhu, and H. B. Sun, “Ultrasensitive temperature sensor based on an isopropanol-sealed optical microfiber taper,” Opt. Lett. 38, 1209 (2013)
7. Y. Li, S. Tan, L. Yang, L. Li, F. Fang, Q. Sun, “Optical Microfiber Neuron for Finger Motion Perception,” Adv. Fiber Mater. **4**, 226-234 (2022).
8. L. Yang, Y. Li, F. Fang, L. Li, Z. Yan, L. Zhang, Q. Sun, “Highly sensitive and miniature microfiber-based ultrasound sensor for photoacoustic tomography,” Opto-Electron Adv **5**, 200076 (2022).
9. H. Dong, L. Chen, J. Zhou, J. Yu, H. Guan, W. Qiu, J. Dong, H. Lu, J. Tang, W. Zhu, Z. Cai, Y. Xiao, J. Zhang, and Z. Chen, "Coreless side-polished fiber: a novel fiber structure for multimode interference and highly sensitive refractive index sensors," Opt. Express 25, 5352-5365 (2017)
10. J. Dong, H. Huang, P. Wu, X. Xiong, J. Tang, H. Guan, W. Zhu, W. Qiu, Y. Zhong, H. Lu, J. Yu, J. Zhang, Z. Chen, and Y. Luo, "Azimuth angle orientation by side scattering for side-polishing of photonic crystal fibers," Opt. Express **25**, 32504-32513 (2017)
11. J. Zhao G. Yin, C. Liao, S. Liu, J. He, B. Sun, G. Wang, X. Xu, Y. Wang, "Rough side-polished fiber with surface scratches for sensing applications," IEEE Photonics Journal 7, 1-7 (2015)
12. J. Tang, J. Zhou, J. Guan, S. Long, J. Yu, H. Guan, H. Lu, Y. Luo, J. Zhang, Z. Chen, "Fabrication of Side-Polished Single Mode-Multimode-Single Mode Fiber and Its Characteristics of Refractive Index Sensing," IEEE J Sel Top Quant **23**, 238-245, (2017)
13. Tiesheng Wu, Yu Shao, Ying Wang, Shaoqing Cao, Weiping Cao, Feng Zhang, Changrui Liao, Jun He, Yijian Huang, Maoxiang Hou, and Yiping Wang, "Surface plasmon resonance biosensor based on gold-coated side-polished hexagonal structure photonic crystal fiber," Opt. Express 25, 20313-20322 (2017)
14. Zhupeng Jiang, Jiangli Dong, Shiqi Hu, Yaxin Zhang, Yaofei Chen, Yunhan Luo, Wenguo Zhu, Wentao Qiu, Huihui Lu, Heyuan Guan, Yongchun Zhong, Jianhui Yu, Jun Zhang, and Zhe Chen, "High-sensitivity vector magnetic field sensor based on side-polished fiber plasmon and ferrofluid," Opt. Lett. 43, 4743-4746 (2018)
15. L. Dong, X. Liu, Y. Zhang, L. Zhuo, D. Li, W. Zhu, H. Zheng, J. Tang, J. Zhang, J. Yu, Z. Chen, "All-fiber multifunctional electrooptic prototype device with a graphene/PMMA (poly(methyl methacrylate)) hybrid film integrated on coreless side-polished fibers", ACS Appl. Electron. Mater. **2**, 447-455 (2020)
16. Teng C., Ying S., Min R., Deng S., Deng H., Chen M., Chu X., Yuan L., Cheng Y., Xue M., “Side-Polish Plastic Optical Fiber Based SPR Sensor for Refractive Index and Liquid-Level Sensing,” Sensors 2022, 22, 6241.
17. Quandong Huang, Lixi Zhong, Jiangli Dong, Ou Xu, Zhaoqiang Zheng, Tianxiong Huang, Jianping Li, Meng Xiang, Songnian Fu, and Yuwen Qin, "All-optical light manipulation based on graphene-embedded side-polished fiber," Opt. Lett. 47, 1478-1481 (2022)
18. Yuchen Wang, Yiwei Li, Yicheng Li, Hao Zhang, Zihan Liu, Yanhong Guo, Zeping Wang, Jun He, Xuhan Guo, Yiping Wang, and Baicheng Yao, "Noise canceled graphene-microcavity fiber laser sensor for ultrasensitive gas detection," Photon. Res. 11, A1-A9 (2023)
19. Linqing Zhuo, Pengpeng Fan, Shuang Zhang, Yuansong Zhan, Yanmei Lin, Yu Zhang, Dongquan Li, Zhen Che, Wenguo Zhu, Huadan Zheng, Jieyuan Tang, Jun Zhang, Yongchun Zhong, Wenxiao Fang, Guoguang Lu, Jianhui Yu, and Zhe Chen, "High-performance fiber-integrated multifunctional graphene-optoelectronic device with photoelectric detection and optic-phase modulation," Photon. Res. 8, 1949-1957 (2020)
20. Y. Wu, B. C. Yao, A. Q. Zhang, X. L. Cao, Z. G. Wang, Y. J. Rao, Y. Gong, W. Zhang, Y. F. Chen, and K. S. Chiang, "Graphene-based D-shaped fiber multicore mode interferometer for chemical gas sensing," Opt. Lett. 39, 6030-6033 (2014)
21. E. Li, X. Wang, and C. Zhang, “Fiber-optic temperature sensor based on interference of selective higher-order modes,” Appl. Phys. Lett, vol. 89, pp. 091119–091121, August 2006.
22. S. Silva, E. G. P. Pachon, M. A. R. Franco, J. G. Hayashi, F. X. Malcata, O. Frazão, P. Jorge, and C. M. B. Cordeiro, “Ultrahigh-sensitivity temperature fiber sensor based on multimode interference,” Appl. Opt, vol. 51, pp. 3236–3242, June 2012.
23. P. Hu, Z. Chen, M. Yang, et al., “Highly sensitive liquid-sealed multimode fiber interferometric temperature sensor,” Sensors and Actuators A: Physical, vol. 223, pp. 114–118, March 2015.
24. H. Fukano, D. Watanabe, and S. Taue, “Sensitivity characteristics of multimode-interference optical-fiber temperature-sensor with solid cladding material,” IEEE Sens. J, vol. 16, pp. 8921–8927, December 2016.
25. Caiyan He, Junbin Fang, Yanan Zhang, Yu Yang, Jianhui Yu, Jun Zhang, Heyuan Guan, Wentao Qiu, Pengjun Wu, Jiangli Dong, Huihui Lu, Jieyuan Tang, Wenguo Zhu, N. Arsad, Yi Xiao, and Zhe Chen, "High performance all-fiber temperature sensor based on coreless side-polished fiber wrapped with polydimethylsiloxane," Opt. Express 26, 9686-9699 (2018)
26. Satyendra K. Mishra, Sandeep N. Tripathi, Veena Choudhary, Banshi D. Gupta, SPR based fibre optic ammonia gas sensor utilizing nanocomposite film of PMMA/reduced graphene oxide prepared by in situ polymerization, Sensors and Actuators B: Chemical 199, 190-200 (2014)
27. B. Sun, F. Li, K. Xu, et al., "Temperature-Insensitive Fiber-Optic Refractometer Based on Immobilization of Polydimethilsiloxane Film," IEEE Photonics Technology Letters, vol. 34, pp. 165-168, February 2022.
28. Ken Kashiwagi and Shinji Yamashita, "Deposition of carbon nanotubes around microfiber via evanascent light," Opt. Express 17, 18364-18370 (2009)
29. Hao Wang, Bohua Chen, X. Zhang, J. Wang, Kan Wu and Jianping Chen, "A new method of ethanol catalytic deposition of MoS2 on tapered fiber for photonic application," 2015 Opto-Electronics and Communications Conference (OECC), Shanghai, China, 2015, pp. 1-3
30. Zhen-Dong Huang, Hao Lu, Kun Qian, Yan-Wu Fang, Qing-Chuan Du, Yan-Bing He, Titus Masese, Xu-Sheng Yang, Yan-Wen Ma, Wei Huang, “Interfacial engineering enables Bi@C-TiOx microspheres as superpower and long life anode for lithium-ion batteries,” Nano Energy, 51, 137-145 (2018)
31. SoonXin Gan, WenSin Chong, ChoonKong Lai, WuYi Chong, Stephen J. Madden, Duk-Yong Choi, Richard M. De La Rue, and Harith Ahmad, "Polarization response of planarized optical waveguides to determine the anisotropic complex refractive index of graphene oxide thin films," Appl. Opt. 61, 744-750 (2022)